Atomic Spectroscopy

Article

Quantitative Analysis of Microstrain and Investigation of Microscopic Mechanism Based on Laser-Induced Breakdown Spectroscopy

Shuoyu Yang, Yazi Wang, Yongyi Du, Jiaqi Zhao, Yue Lv, Xiaoning Yang, Yifan Luo, and Ruibin Liu *

Key Lab of Precision Spectroscopy and Optoelectronic Technology, School of Physics, Beijing Institute of Technology, Beijing 100081, P. R. China

Received: *July 10, 2026;* ***Revised:*** *August 18, 2026;* ***Accepted:*** *August 19, 2026;* ***Available online:*** *August 19, 2026.*

DOI: 10.46770/AS.2026.0055

ABSTRACT: The microstructure of metallic materials, particularly their strain characteristics, constitutes the core determinant of macroscopic physicochemical properties; therefore, achieving rapid, precise, and in-situ characterization of microstructure is important for research on metallic materials. Since the microstructure of materials can modulate plasma excitation conditions, microstrain information in metallic materials can be reflected through plasma emission spectra. Laser-induced breakdown spectroscopy (LIBS) has been conventionally employed for detecting elemental composition and conducting quantitative analysis of elemental content; however, investigations of microstrain based on LIBS remain unreported. In this study, we, for the first time, utilized spectroscopic information from laser-induced plasma to establish a classification model for microstrain. Furthermore, by integrating artificial intelligence algorithms, we constructed a quantitative relationship model between spectral characteristics and microstrain, thereby realizing online in-situ quantitative analysis of microstrain. We also conducted an in-depth investigation into the influence mechanism of microstructure on plasma spectra, providing a solid theoretical and experimental foundation for rapid diagnosis of material microstrain based on LIBS technology.

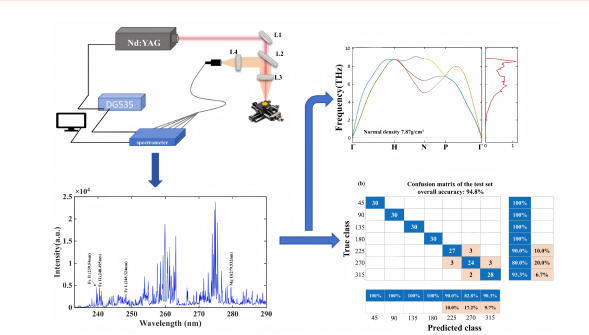

INTRODUCTION

The microstructure of materials constitutes the core determinant of their macroscopic physicochemical properties; achieving rapid, precise, and in-situ characterization of microstructure has remained a critical scientific issue in the fields of materials science and analytical techniques. The microstructure of materials modulates plasma excitation conditions, ultimately imprinting characteristic signals in LIBS spectra that can be utilized to discriminate among different microstructural states[1-2]. In 2010, Pan Shenghua et al. investigated the influence of metallographic microstructure on LIBS spectra. The results demonstrated that, under identical experimental conditions, the pearlite-ferrite microstructure exhibited the highest overall spectral intensity, followed by the bainitic microstructure, while the martensitic microstructure displayed the lowest spectral intensity. This study indicates that LIBS spectra can sensitively capture metallographic information of steel, and that a complex yet robust correlation exists between spectral characteristics and microstructure types[3]. Previous studies have also revealed linear correlations between microstructural parameters—including grain size, crystal structure, phase fraction and distribution, and dislocation density—and plasma spectral characteristics. Harse Sattar et al. proposed that microstructure and electronic properties directly influence the electron temperature in laser ablation plasma, with the average ablation rate progressively decreasing from soft to hard materials[4] .In certain instances, samples with similar macroscopic compositions may exhibit variations in spectral signals under laser irradiation due to disparities in local composition and mechanical properties. Galmed et al. observed a strong linear correlation between plasma temperature and Vickers hardness[5]. In 2025, Zhang et al. investigated the formation mechanism of lattice defects in black silicon and their manifestation in optical spectra, discovering that amorphization modulates laser-material interactions and plasma characteristics by altering surface

structure and chemical states of the specimen, thereby elevating the intensity of characteristic LIBS peaks. This finding demonstrates that LIBS spectra can effectively reflect crystallographic phase information of materials[6]. The aforementioned studies did not encompass applications of LIBS to microstrain measurement; however, their results indicate that the relative distribution of LIBS spectral intensities is constrained by microstructural effects, providing a research foundation for the acquisition of spectral signatures under microstrain conditions through the integration of LIBS technology and artificial intelligence approaches.

When a high-energy laser beam irradiates the sample surface, the laser energy rapidly ablates and vaporizes the local material within an extremely short temporal interval. The resulting atoms and molecules initially generate nascent free electrons through multiphoton or cascade ionization. Subsequently, these free electrons continuously absorb photon energy and are accelerated under the sustained action of the laser field, subsequently colliding with lattice atoms; the impacted atoms, upon acquiring sufficient energy, undergo re-ionization, releasing additional electrons[7-8]. The newly generated electrons are likewise accelerated and continue to collide with additional atoms, establishing a characteristic avalanche effect that produces a substantial population of charged ions within sub-microsecond time scales, ultimately constituting a high-temperature, high-density plasma. Modifications in microstructure—including grain size, phase composition, dislocation density, and related parameters—induce alterations in the crystal lattice (lattice constants, interatomic bonding configurations, electronic structure, etc.), thereby affecting plasma excitation characteristics (plasma temperature, electron density, etc.)[9–11] . Consequently, plasmas generated from distinct lattice structures exhibit discernible differences in spectral emission intensity, characteristic peak positions, and linewidths[12-13] .The microstructure of materials can modulate plasma excitation conditions, resulting in complex yet robust correlations between LIBS spectra and crystalline phases, phase transformations, defects, or microstructural types. This interdependence reveals the microstructural state of materials, establishing a closed-loop relationship of "microstructure ↔ plasma characteristics ↔ spectral response[14–17] .

Based on the interaction between high-energy lasers and metallic materials, this study elucidates the mechanistic relationship between plasma spectra and the microstructure of metallic materials, thereby establishing a correlation between "spectra ↔ microstructure." Based on critical plasma characteristic parameters including plasma temperature and electron number density, the mechanism of laser-metal interaction is thoroughly analyzed. Furthermore, the influence of distinct microstructures on plasma spectral features is investigated, and the correlation between crystallographic information and spectral signatures is established accordingly. At the atomic level, the pulse evolution patterns of different atomic characteristic peaks are studied through high-resolution spectral analysis to elucidate the mechanism by which plasma spectra reflect material composition and microstructural information. High-precision models are subsequently constructed utilizing spectral data, providing a reference for the application of LIBS technology in material microstructure characterization.

EXPERIMENTAL

Samples. This experiment employed high-purity iron sheets (Fe content ≥ 99.9%) purchased from Qinghe County Tengfeng Metal Materials Co., Ltd. (Fig. S1). To facilitate strain application for bending to specific angles, we prepared all samples with dimensions of 100 mm × 100 mm × 0.5 mm. We fabricated seven samples with fixed bending angles: we subjected samples within the 45°–135° range to compressive strain and those within the 225°–315° range to tensile strain. The micro-strain values of the samples were obtained through strain gauge measurements. Fig. 1 illustrates the variation of strain with bending angle. Smaller bending angles below 180° induce increased compressive strain, while larger bending angles above 180° produce greater tensile strain (microstrain values increase sequentially from sample W-1 to W-7). An approximately linear relationship exists between surface microstrain and bending angle in the metallic samples. However, because maintaining perfect consistency during the bending process proves difficult, slight deviations in bending angle also cause variations in microstrain; consequently, some bending angles and their corresponding microstrain values deviate from the fitted line. During the experiments, the bending angle of each sample was verified immediately after bending using an angle gauge, and this verification was performed both before and after the LIBS measurements to ensure that the angular deviation remained within ±0.5°.

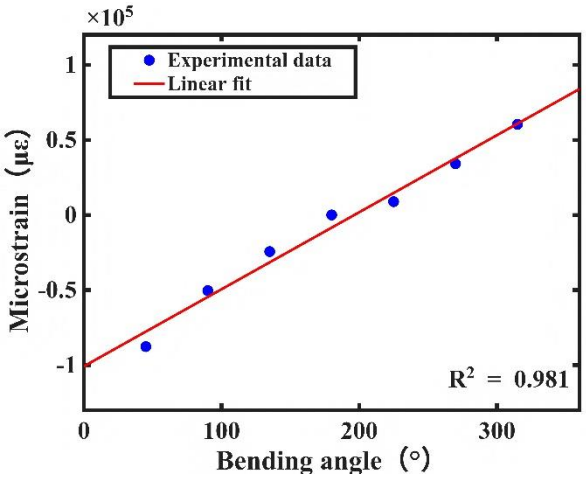

Fig. 1 Variation of microstrain with bending angle.

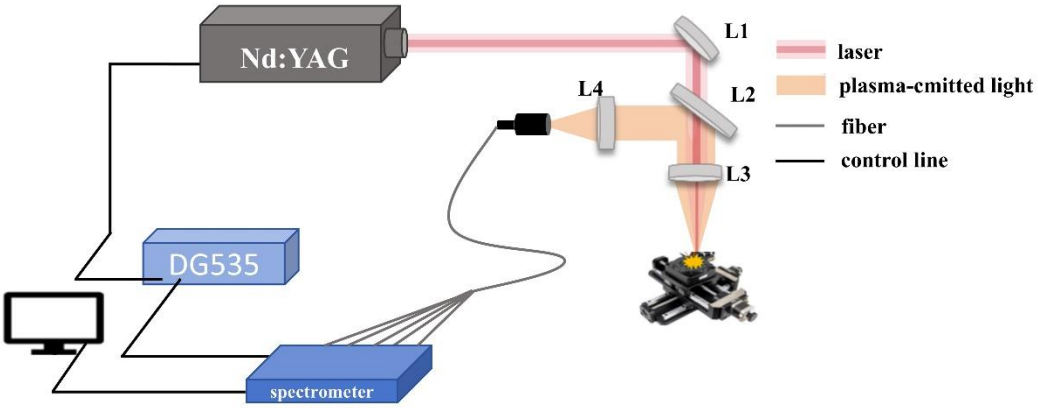

Fig. 2 Schematic diagram of the laser-induced breakdown spectroscopy detection system.

Experimental setup. Fig. 2 illustrates the experimental setup, which primarily comprises a laser-induced breakdown spectroscopy excitation module, a spectral collection module, and a delay control module. The LIBS excitation module employs a Q-switched Nd:YAG pulsed laser (NewWave, USA) as the excitation source to ablate samples, operating at a wavelength of 1064 nm, pulse width of 5 ns, adjustable repetition rate of 1–10 Hz, maximum single-pulse output energy of 110 mJ, and spot diameter of 5 mm. The laser emits a pulsed laser beam, which first passes through mirror L1 to alter the propagation direction, then traverses a plano-convex fused silica lens L3 with a focal length of 100 mm to focus the laser 3 mm beneath the sample surface for sample excitation and plasma generation. The spectral collection module employs a fiber spectrometer with a resolution better than 0.1 nm. The laser-induced plasma passes through a focusing lens, a 45°-inclined dichroic mirror L2 (high transmission at 1064 nm, high reflection for visible light), and a plano-convex fused silica lens L4 with a focal length of 100 mm, and we couple it into a one-to-seven fiber bundle. The delay control module manages the overall timing sequence of all modules through a digital delay generator (DG535, Stanford Research Systems). We employ a three-dimensional translation stage to control the sample excitation positions, forming an ablation crater matrix on the sample surface to acquire multiple sets of spectral data for each sample. To prevent surface height variations upon sample replacement from compromising experimental stability, we employ a laser positioning device to maintain consistent surface heights across different samples. Simultaneously, to ensure stability of the laser energy delivered to the sample surface, we utilize a dust extraction apparatus throughout the experiment to absorb particulate matter generated from laser ablation of the sample surface.

We acquired all spectral data under identical laser parameters: laser energy of 31.5 mJ, spectral acquisition delay time of 1.5 μs, and integration time of 30 μs. We collected 60 laser pulse signals at each sampling position, irradiating three distinct positions on each sample, ultimately obtaining 180 spectral files per sample.

RESULTS AND DISCUSSION

Spectral Classification and Quantitative Analysis of Microstructure Evolution. When the laser pulse focuses on the sample surface, energy injection induces sample ablation and ionization, generating a high-temperature, high-pressure plasma. During plasma cooling, excited atoms and ions undergo transitions to lower energy levels, emitting radiant light at characteristic wavelengths. The collection system gathers this radiant light and directs it into the spectrometer for dispersion, and the detector records the signal to obtain the characteristic spectrum of the sample. Analyzing these radiation spectra enables us to obtain elemental information from the sample. Fig. 3 presents the characteristic spectra of the sample in the 200–900 nm wavelength range, with characteristic peaks of major elements labeled to facilitate subsequent investigation of the variation patterns in peak intensities.

To further achieve classification and quantitative analysis of samples with different microstructures through spectroscopy, we investigated the characteristic peak intensities and the pulse evolution patterns of characteristic peaks for samples with distinct microstructures. Fig. 4 presents the intensity comparison of typical characteristic peaks across samples with different bending angles after we discard the first ten unstable pulses at each position. The Hα characteristic peak intensity shows no significant variation among metallic samples with different microstructures, whereas the N I peak at 746.83 nm, the O I peak at 777.19 nm, and the O I peak at 844.64 nm all exhibit decreasing intensity with increasing bending angle. These observations demonstrate that characteristic peak intensities differ among samples with distinct microstructures, indicating that plasma spectra can reflect variations in material microstructure and establishing a foundation for classifying samples with different microstructures through spectroscopic analysis (Fig. S2).

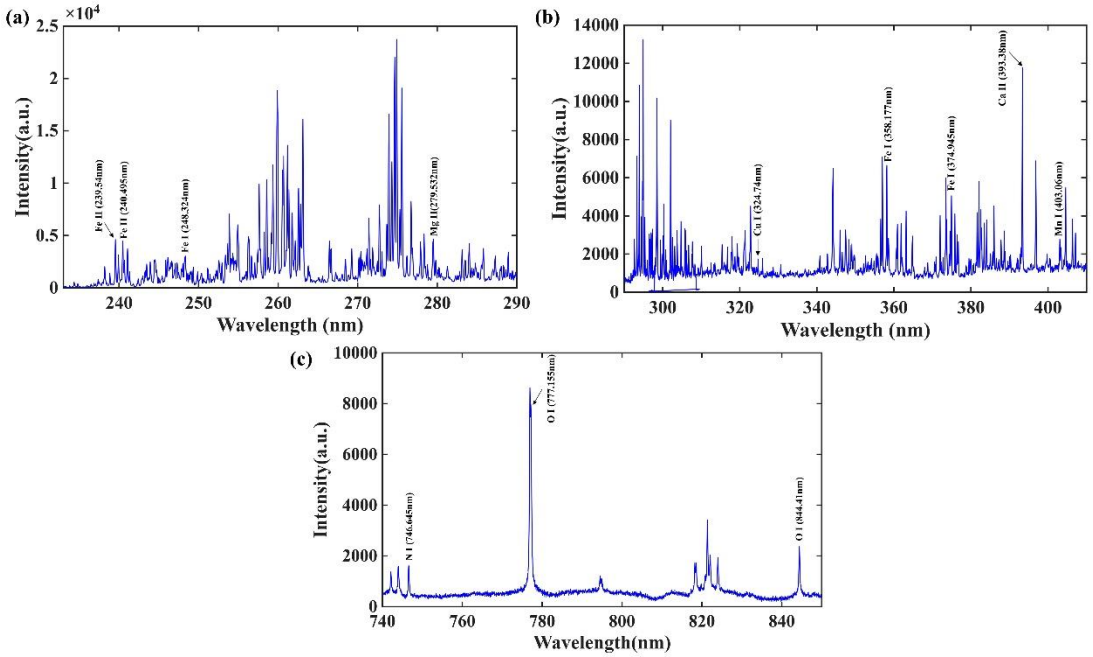

Fig. 3 Characteristic spectrum of the sample. (a)230nm-290nm. (b)290nm-410nm. (c)740nm-845 nm.

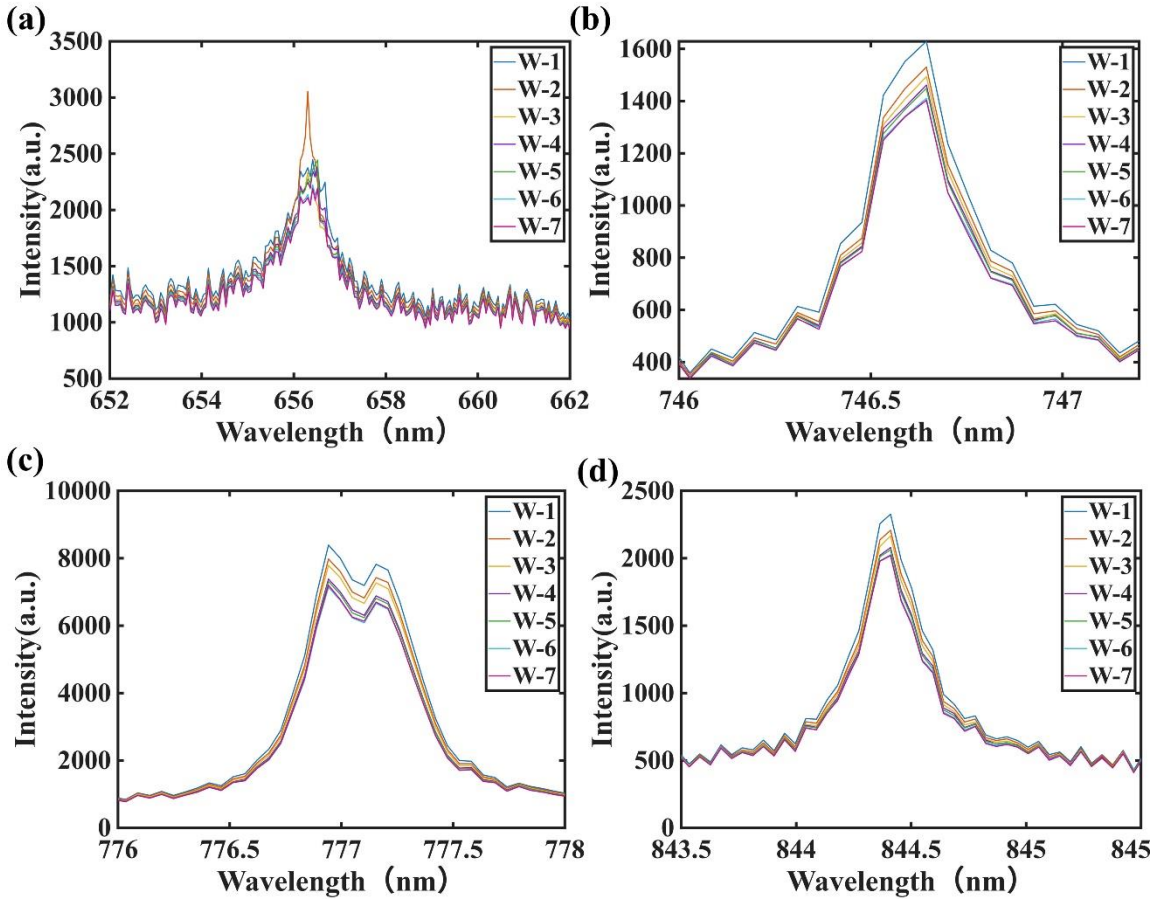

Fig. 4 Characteristic peaks of samples with different bending angles: (a) 656.28 nm Hα, (b) 746.83 nm N I, (c) 777.19 nm O I, (d) 844.64 nm O I.

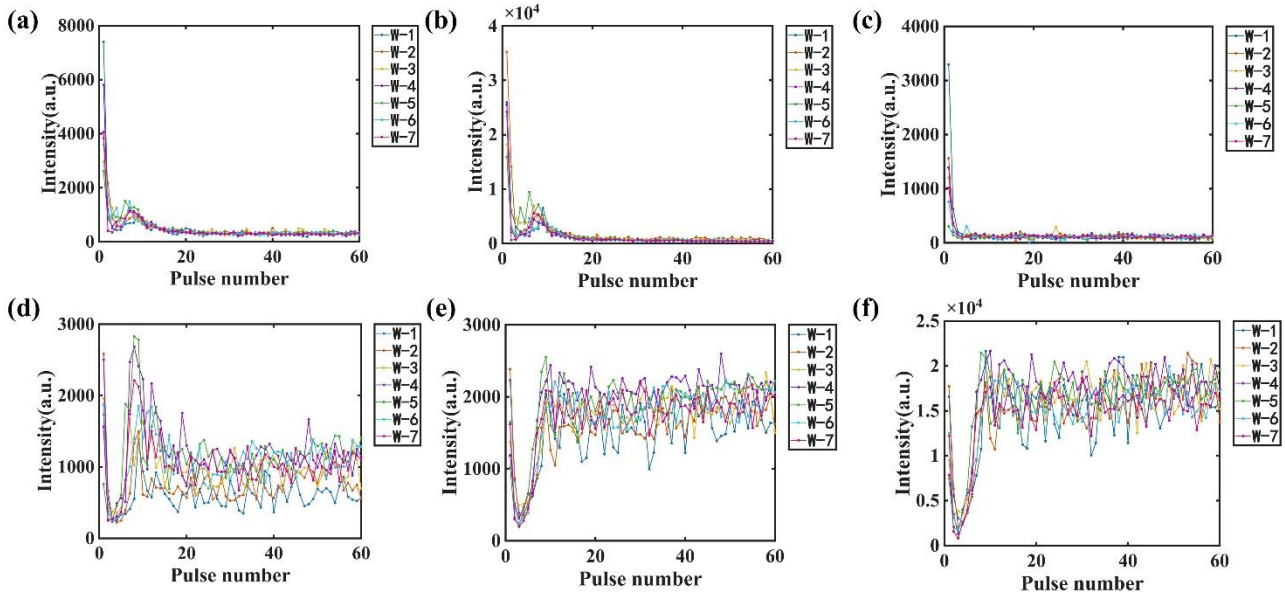

Fig. 5 Variation of characteristic peak intensity with pulse number for background-subtracted spectra of samples with different bending angles: (a) 279.55 nm Mg II, (b) 393.37 nm Ca II, (c) 589.00 nm Na I, (d) 403.08 nm Mn I, (e) 324.75 nm Cu I, (f) 358.12 nm Fe I.

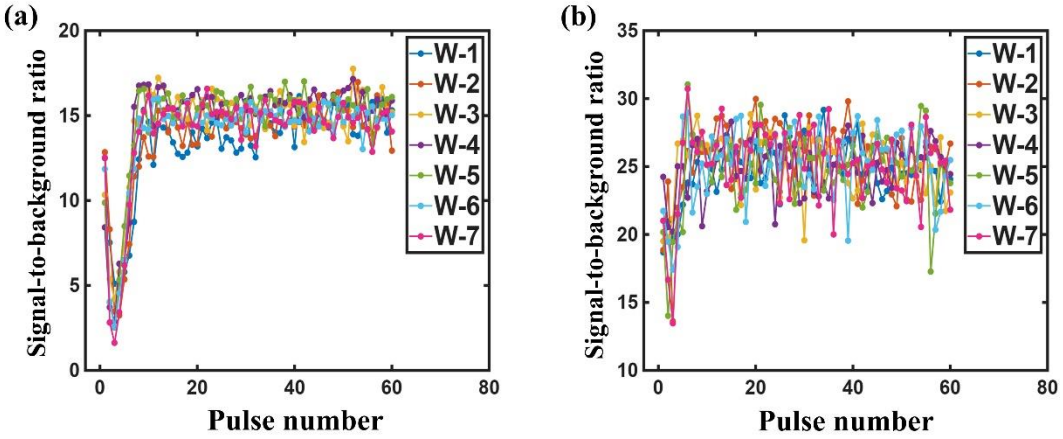

Fig. 6 Variation of characteristic peak signal-to-background ratio with pulse number: (a) 358.12 nm Fe I, (b) 263.10 nm Fe II.

Figure 5 presents the variation of background-subtracted spectral characteristic peaks with pulse number. We observe that elemental characteristic peaks exhibit large intensity fluctuations during the first ten pulses, with abrupt rises and falls, and essentially stabilize after the tenth pulse. Among these, Mg and Na essentially disappear after the third pulse, and the characteristic peak intensity of Ca II at 393.37 nm also undergoes a cliff-like decline at the second pulse before gradually vanishing. This indicates that spectra from the first three pulses suffer from interference by surface oxide layers and contaminants on the sample; only the variation patterns of characteristic peak intensities after we exclude these initial three pulses can represent the true condition of the sample itself. After the third pulse, characteristic peaks of Mn, Cu, and Fe all exhibit a pattern of initial rise followed by stabilization. Characteristic peaks of most elements stabilize after ten pulses.

The characteristic peaks of samples in this experiment are relatively dense; therefore, we calculate the signal-to-background ratio as the ratio of the background-subtracted net peak intensity to the fitted background signal intensity. We select the strong atomic peak of Fe at 358.12 nm and the ionic peak at 263.10 nm to investigate the variation of signal-to-background ratio with pulse number. As Fig. 6 illustrates, the spectral signal-to-background ratio achieves high values and stabilizes after ten pulses.

Based on our preceding investigations into the variation patterns

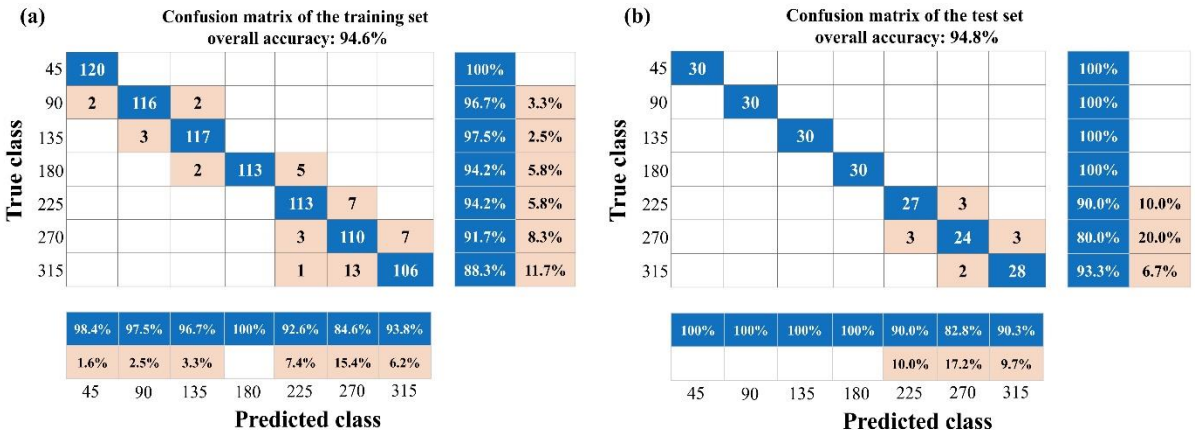

Fig. 7 (a) confusion matrix of the training set for the classification model using spectra remaining after removing the first ten pulses, (b) confusion matrix of the test set for the classification model using spectra remaining after removing the first ten pulses.

of background signal intensity, plasma temperature, characteristic peak intensity, and signal-to-background ratio with pulse number, we establish classification models using both the complete spectral dataset and the spectral data remaining after we remove the first ten pulses at each position. The classification model was constructed using linear discriminant analysis (LDA). The training and test sets were partitioned as follows. A total of 180 spectra were recorded for each sample, corresponding to three spatial positions with 60 laser pulses per position. Following the removal of the initial 10 pulses, 150 spectra per sample were retained. Subsequently, 120 spectra were randomly selected from each sample to form the training set, with the remaining 30 spectra allocated to the test set. Fig. 7 presents the model results: the training set classification accuracy improves from 89.1% for the complete spectral model to 94.6% for the model with the first ten pulses removed, while the test set classification accuracy increases from 90.9% to 94.8%. The classification errors primarily occur between adjacent samples with small angular differences, and removing the first ten unstable pulses enhances classification accuracy.

Based on the aforementioned findings that the remaining spectra stabilize after we remove the spectral data of the first ten pulses at each position, we select the stabilized spectral data to establish a strain quantitative model. Fig. 8 presents the model results[18]. Analyzing the quantitative metrics, the model demonstrates exceptional performance on the training set, achieving a coefficient of determination R^2 of 0.997 and a root mean square error RMSE of merely 2583.821 microstrain; it also exhibits excellent performance on the test set, with R^2 of 0.923 and RMSE of 8202.906 microstrain. Both sets of data points cluster tightly around the diagonal line, indicating that the model has already captured the primary characteristic patterns of the samples during the learning phase. Overall, the model not only possesses excellent fitting capability but also maintains extremely high prediction

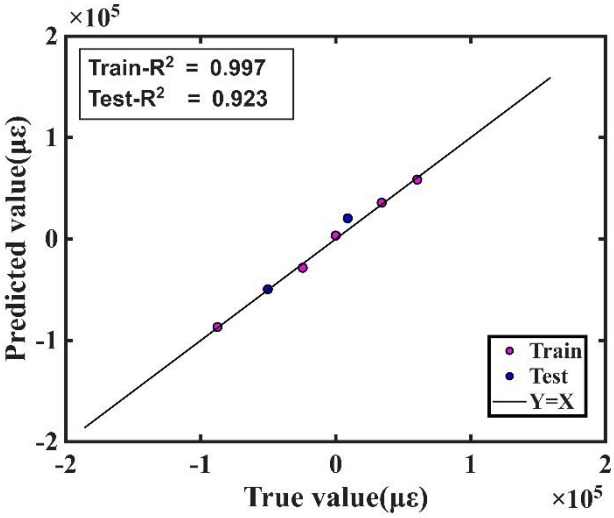

Fig. 8 Strain quantitative analysis model based on PCA-PLS.

accuracy without exhibiting overfitting phenomena, enabling reliable prediction of material strain behavior. Given that the samples investigated in this study possess identical material composition and that their strain differences only induce subtle variations in microstructural organization, this study elucidates the high sensitivity and effectiveness of plasma emission spectroscopy in capturing differences in material microstructure.

Investigation of Plasma Parameter Variation Mechanisms Under Different Microstructural Changes. Based on the high-precision classification models constructed from spectra of samples with different microstructures in the aforementioned studies, we observe that laser-induced plasma technology can sensitively capture differences in sample microstructure, while also demonstrating that laser-induced plasma spectral responses

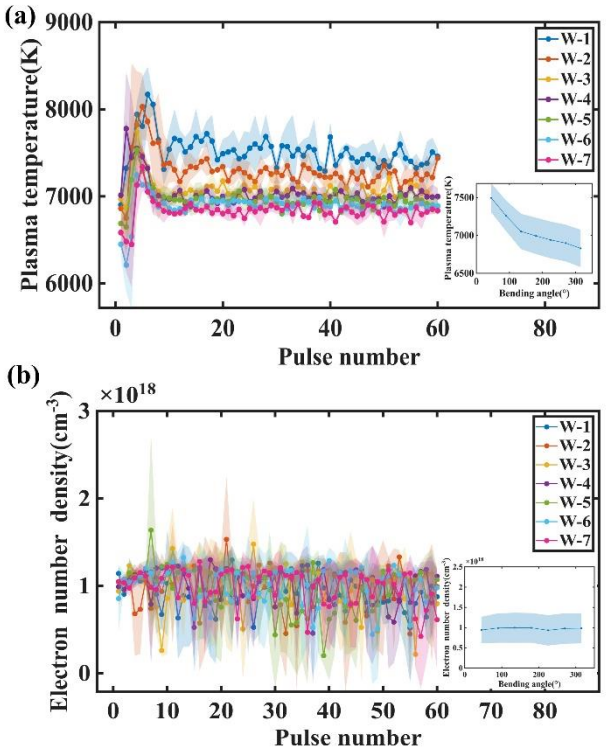

Fig. 9 (a) Variation of plasma temperature with pulse number; (b) variation of electron number density with pulse number.

Table 1. Characteristic Spectral Line Parameters of Fe

Peak wavelength λ (nm)	$g_k A_{ki}(S^{-1})$	E_k(eV)
Fe I 358.119	1.33×10^{9}	4.32
Fe I 371.993	1.78×10^{8}	3.33
Fe I 374.948	6.87×10^{8}	4.22
Fe I 385.991	8.72×10^{7}	3.21

can map microscopic variations such as crystal defects and dislocations. To investigate the response mechanisms of laser-induced plasma to different microstructures, we conducted studies on plasma characteristics.

Through investigating plasma characteristics, we can elucidate the process of laser-sample interaction and subsequently analyze the spectral properties of each sample. We characterize plasma properties through plasma temperature and electron number density; in LIBS research, we determine plasma temperature using the Boltzmann plot method[19] and derive electron number density through Lorentzian fitting of the Hα peak [20]. In this study, the emission lines of Fe were selected for constructing the Boltzmann plot (Fig. S3), and the required spectroscopic parameters were obtained from the NIST (National Institute of Standards and Technology) Atomic Spectra Database, as listed in Table 1. On this basis, we plot the variation of plasma temperature and electron number density with pulse number. As Fig. 9 (a) illustrates, for the first ten pulses at each position, the plasma temperature exhibits a variation pattern of initial increase followed by decrease, while the plasma temperature of subsequent pulses gradually stabilizes. The variation pattern of the first ten pulses primarily originates from the influence of surface contaminants and oxide layers on the sample; therefore, in subsequent analyses, we remove the spectral data of the first ten pulses to eliminate interference from surface contaminants and oxide layers. As the inset in Fig. 9(a) shows, after removing the spectral data of the first ten pulses, the plasma temperature of the remaining spectra decreases with increasing bending angle. Regarding electron number density, as Fig. 9(b) illustrates, it exhibits certain fluctuations but overall trends toward stability. As the inset in Fig. 9(b) shows, after we remove the first ten spectral data points, the electron number density still shows no significant variation across different bending angles.

The research samples in this experiment possess identical material composition, differing only in bending angle. Compression and tension of the samples introduce microstrain and consequently alter the microstructure of the material. To investigate the relationship between microstrain and plasma characteristic parameters, we plot the relationships between microstrain and plasma temperature, electron number density, and background average intensity, respectively. As Fig. 10(a)–(c) illustrate, microstrain exhibits good linear correlations with both background average intensity and plasma temperature ($R^2 = 0.845$ and 0.932, respectively), whereas the linear relationship with electron number density remains weak ($R^2 = 0.055$). Given the mutual influence among various plasma parameters, we establish a multiple linear regression model for microstrain based on plasma temperature, electron number density, and background average intensity. Fig. 10(d) presents the results: the R^2 between measured microstrain and fitted values improves to 0.970, significantly surpassing the single-factor fitting results. This indicates that the influence mechanism of microstrain on plasma characteristics is rather complex; background average intensity, plasma temperature, and electron number density couple with each other and collectively respond to variations in microstrain. A single parameter cannot adequately describe this intrinsic relationship, necessitating multi-parameter synergistic analysis to accurately characterize the quantitative relationship between microstrain and plasma state.

Through the above analysis, we find that under both compressive and tensile strain conditions, the sample exhibits no obvious variation in electron number density. Therefore, the core mechanism dominating background signal variation does not originate from minute differences in original electron concentration; rather, microstructural differences—including strain energy storage in compressed regions and microcrack energy dissipation in tensile regions—modulate laser-material interaction efficiency and subsequent plasma thermodynamic evolution. Tensile deformation induces microcracks and pores,

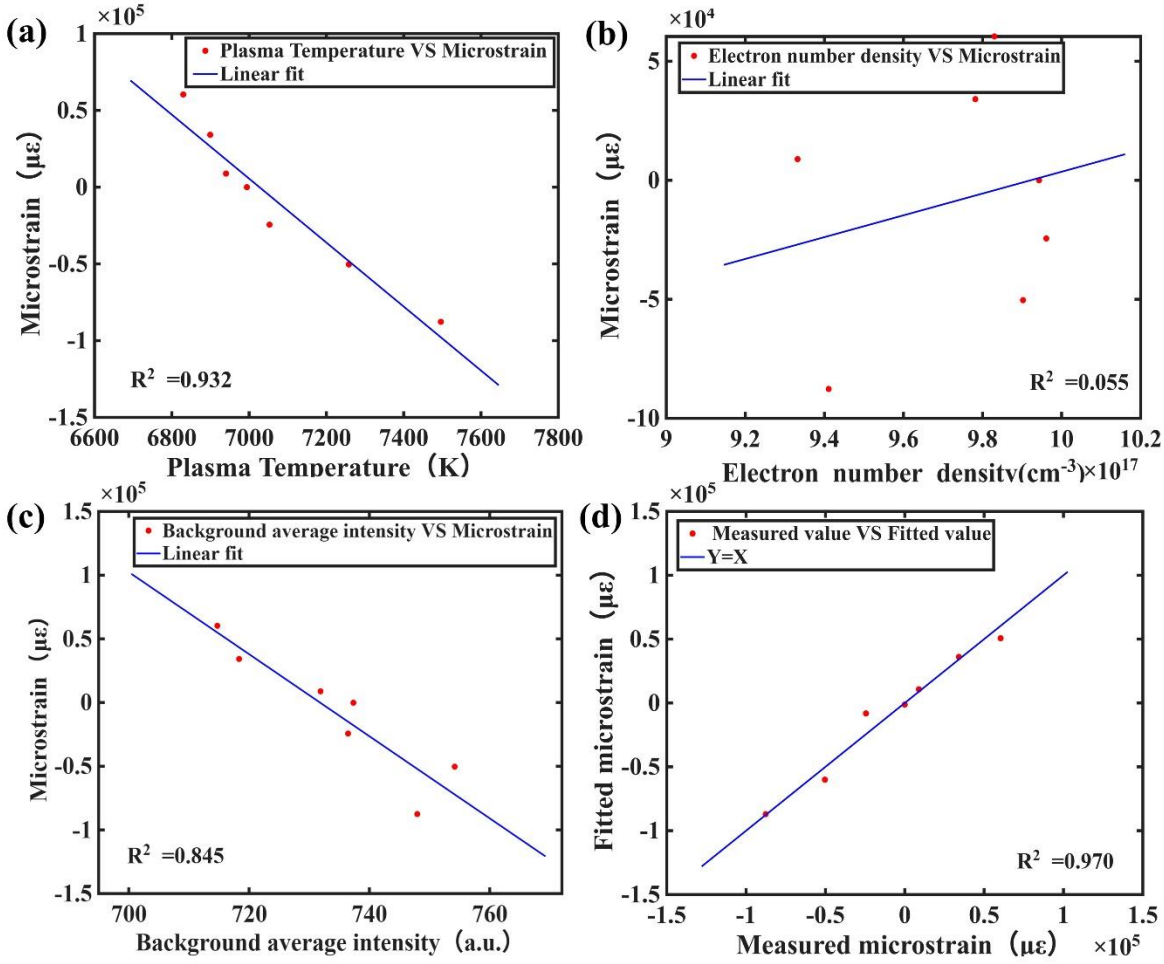

Fig. 10 (a) Relationship between microstrain and plasma temperature; (b) relationship between microstrain and electron number density; (c) relationship between microstrain and background average intensity; (d) comparison between measured microstrain values and predicted values from the multiple linear regression model (established based on plasma temperature, electron number density, and background average intensity).

and the resulting disruption of material continuity partially dissipates laser energy through material ejection and heat loss at crack surfaces. This reduction in effective energy available for sustaining high plasma temperatures leads to decreased plasma temperature[21-22]. Compression deformation causes a sharp increase in dislocation density and lattice densification. These changes enhance electron-phonon coupling efficiency and optical absorptivity, thereby improving the conversion efficiency of laser energy into plasma thermal energy and leading to elevated plasma temperature[23-24] . Although electron number density shows no significant variation, the elevated temperature still enhances background radiation intensity through intensified electron thermal motion and blackbody radiation efficiency, manifesting as increased continuous background signal. The variation patterns of plasma temperature and background signal intensity with pulse number during the first ten pulses exhibit opposite trends, because during the initial laser cleaning stage, surface contaminants, oxide layers, and adsorbates on the sample undergo preferential ablation. The spectral signals from these impurities dominate the influence on the background signal, temporarily masking the intrinsic correlation between the plasma temperature and the background signal, a correlation determined by microstructural changes in the bulk material. After surface cleaning, this correlation becomes apparent.

Elucidation of Lattice Distortion–Phonon Dynamics–Plasma Coupling Mechanism Under Microstructure Evolution. For metallic samples with identical material composition, compression and tension operations induce changes in material microstructure. Compression reduces interatomic spacing in the crystal lattice and increases coordination number, leading to material densification; tension introduces microcracks and pores, causing lattice expansion and structural loosening. This density difference affects plasma characteristics: high-density samples exhibit shortened interatomic spacing, and laser energy undergoes absorption by free electrons within a shorter skin depth (increased

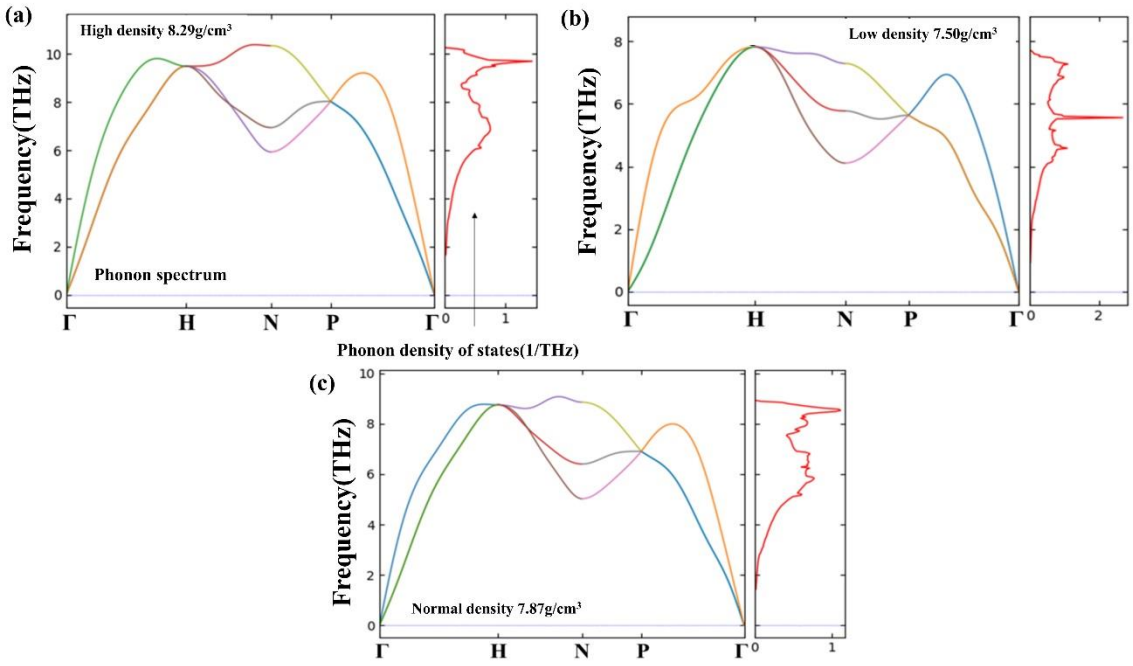

Fig. 11 Phonon dispersion relations and phonon density of states for Fe material under different density conditions: phonon dispersion curves (left) and corresponding phonon density of states as a function of frequency (right) for (a) high density (8.29 g/cm³), (b) low density (7.50 g/cm³), and (c) normal density (7.87 g/cm³).

optical absorptivity), enhancing energy deposition density and yielding higher plasma temperatures[25] . Furthermore, differences in lattice vibration characteristics (phonon spectra) affect the electron-phonon coupling efficiency, thereby modulating the thermodynamic evolution of the plasma. To deeply reveal the microscopic dynamic mechanism underlying the plasma temperature difference, the study further performs first-principles calculations of the phonon dispersion curves and the phonon density of states (PDOS) of Fe materials under different density conditions, including the high-density compressed sample (8.29 g/cm³) and the low-density stretched sample (7.50 g/cm³), using the normal-density sample (7.87 g/cm³) as the control group.

We perform phonon spectrum calculations using the finite displacement method combined with ABACUS and Phonopy programs. We select a primitive cell containing 2 Fe atoms to construct a 4×4×4 supercell (128 Fe atoms total) as the calculation model. We calculate atomic forces using the PBE functional combined with the linear combination of atomic orbitals (LCAO) method, adopt a 4×4×4 k-point grid sampling for Brillouin zone integration, and set the self-consistent field iteration energy convergence threshold to 1×10^{-7} eV. The calculations fully account for the magnetic characteristics of Fe material, employing spin-polarized treatment to accurately describe its ferromagnetic ground state. We calculate the force constant matrix through the finite displacement method, subsequently solve the dynamical matrix to obtain phonon dispersion curves and phonon density of states. Fig.11 presents the calculated phonon dispersion relations and phonon density of states for Fe material under different density conditions The results show that lattice density modulates the phonon spectral distribution, which provides a valuable lattice dynamics perspective for understanding the electron-phonon coupling efficiency and energy transport processes, , thereby providing a lattice dynamics basis for understanding the microstructural dependence of the plasma temperature.

The phonon spectra in Fig. 11 reveal density-dependent lattice dynamic differences, which directly affect the energy conversion process after plasma formation. As shown in Fig. 11(a), the phonon dispersion curves of the high-density sample (8.29 g/cm³) exhibit an overall blue shift, and the PDOS on the right shows the main peak shifting toward high frequencies, indicating enhanced interatomic bonding strength. This behavior is reasonably interpreted as suggesting enhanced electron-phonon coupling, where the electron kinetic energy from laser deposition may convert more efficiently into lattice thermal energy, raising the initial plasma temperature. Sharp high-frequency peaks suggest a high degree of vibrational mode localization, which is likely to reduce phonon-phonon scattering probability and extend nonequilibrium phonon lifetimes. Such localization is also expected to restrict phonon mean free paths and suppress initial thermal diffusion, causes laser-deposited heat to concentrate more in the interaction region, and reduces heat dissipation to surrounding material. The plasma temperature obtained through

the Boltzmann plot method is significantly higher than that of the stretched sample. In contrast, the low-density sample (7.50 g/cm³) in Fig. 11(b) exhibits a redshift characteristic in the phonon dispersion curves, with relatively flattened dispersion curves (softening of the acoustic branches). The PDOS shows an increased weight in the low-frequency region, while the high-frequency peak intensity decreases and broadens, suggesting that lattice expansion is physically associated with weakened interatomic coupling, weaker electron-phonon coupling, and potentially enhanced anharmonic effects. As shown in Fig. 11(c), the phonon spectra of the normal-density sample (7.87 g/cm³) display characteristics intermediate between those of the high- and low-density samples, with both the frequency distribution and the PDOS peak shapes showing a moderate degree, reflecting typical vibration characteristics under a standard lattice structure [26–30].

Through the analysis of Fig. 11, we find that changes in lattice density significantly alter the force constant matrix and the phonon density of states distribution by modulating the interatomic spacing and coordination environment. In the compressed sample (high density), the high-frequency localized phonon modes are reasonably considered to enhance electron-phonon coupling and suppress the initial diffusion of laser-induced thermal energy, resulting in a higher plasma temperature. The phonon softening and enhanced anharmonic effects (increased phonon-phonon scattering probability) in the stretched sample (low density) are likely to promote rapid initial energy dissipation, leading to a lower plasma temperature. Based on these trends, this finding helps construct a conceptual physical picture of "microstructure–phonon dynamics–plasma thermodynamic state" and elucidates the lattice dynamic mechanism by which strain-induced microstructural differences modulate the plasma temperature.

CONCLUSION

In this study, we propose and validate an in-situ quantitative analysis method for metallic microstrain based on laser-induced breakdown spectroscopy combined with machine learning algorithms. Through LIBS experiments on metallic samples with different microstructures, we established a high-accuracy classification model with an accuracy of 94.8% and a quantitative model for microstrain with an R^2 of 0.923 using the stable spectra, confirming the feasibility and high precision of this method for in-situ detection of metallic microstrain. Analysis of plasma parameters reveals that microstrain exhibits a strong linear correlation with plasma temperature, while showing a weaker correlation with electron number density, indicating that the spectral response mechanism originates from the laser–material interaction efficiency modulated by microstructural differences and the subsequent thermodynamic evolution of the plasma. We also analyze phonon dispersion curves and phonon density of states images for Fe material under different density conditions, thereby explaining the variation patterns of plasma temperature from the microscopic perspective.

In summary, this study systematically reveals the mechanisms by which plasma spectral parameters reflect the evolution of material microstructure. The elevation or reduction of plasma temperature, the variation of characteristic peak intensities, and the multi-parameter coupling relationships all fundamentally originate from changes in lattice density, bonding energy, and electron-phonon coupling state at the microscopic level. This conclusion not only deepens the understanding of laser-material interaction mechanisms but also provides a solid theoretical and experimental foundation for rapid diagnosis of material microstrain based on plasma spectroscopy technology. Metal bending gives rise to geometric and surface effects in addition to microstructural alterations. While various countermeasures were adopted in the present study to mitigate these factors, complete elimination of their influence remains unattainable. Consequently, in subsequent investigations, three-dimensional surface characterization techniques will be employed to enable a more quantitative differentiation between the contributions of microstructural and geometric effects to the LIBS signal response. Meanwhile, multiple parallel samples will be added at each strain level to further validate the generalization ability and robustness of the model.

ASSOCIATED CONTENT

The supporting information (Figs S1−S3) is available at https://www.at-spectrose.com

AUTHOR INFORMATION

Ruibin Liu received his Ph.D. degree from the Institute of Physics, Chinese Academy of Sciences, in 2007. He is currently a professor at the School of Physics, Beijing Institute of Technology. His research interests cover a broad range of areas, including laser-based material identification, novel photoelectric detection technologies, and the industrial applications of laser spectroscopy and photoelectric sensing techniques.

Corresponding Author

* R. B. Liu

Email address: liusir@bit.edu.cn

Notes

The authors declare no competing financial interest.

ACKNOWLEDGMENTS

The authors gratefully thank the National Key Research and Development Program (2023YFC301 0603) for financial support of this work.

REFERENCES

1. M. Cui, G. Shi, L. Deng, H. Guo, S. Xiong, L. Tan, C. Yao, D. Zhang, and Y. Deguchi, *J. Anal. At. Spectrom*., 2024, **39,** 1361-1374. https://doi.org/10.1039/d3ja00453h
2. J. H. Kim and H. W. Choi, *Photonics*, 2025, **12,** 1220**.** https://doi.org/10.3390/photonics12121220
3. S. H. Pan, J. D. Lu, S. C. Yao, M. C. Jiang, and P. Li, *Chin. J. Lasers*, 2010, **37,** 2126-2130. https://doi.org/10.3788/CJL20103708.2126
4. H. Sattar, Z. Hu, F. Guan, S. Shi, D. Zhang, M. Imran, Z. Tang, L. Guo, and W. Luo, *J. Alloys Compd*., 2023, **947,** 169240. https://doi.org/10.1016/j.jallcom.2023.169240
5. A. H. Galmed, C. M. Steenkamp, I. Ahmed, H. Von Bergmann, M. A. Harith, and M. Maaza, *J. Laser Appl*., 2020, **32,** 012012. https://doi.org/10.2351/1.5122751
6. X. Zhang, W. Li, C. Jin, F. Liu, N. Wei, R. Zhou, X. Zhu, and W. Zhao, *Opt. Laser Technol*., 2025, **192,** 113534. https://doi.org/10.1016/j.optlastec.2025.113534
7. A. De Giacomo, M. Dell'Aglio, O. De Pascale, R. Gaudiuso, V. Palleschi, C. Parigger, and A. Woods, *Spectrochim. Acta, Part B*, 2014, **100,** 180-188. https://doi.org/10.1016/j.sab.2014.08.013
8. J. Yu, Q. Ma, V. Motto-Ros, W. Lei, X. Wang, and X. Bai, *Front. Phys*., 2012, **7,** 649-669. https://doi.org/10.1007/s11467-012-0251-2
9. Y. Dai, J. Li, W. Zhong, X. Dong, W. Li, S. Yao, and J. Lu, *Acta Opt. Sin*., 2014, **34,** 330003. https://doi.org/10.3788/AOS201434.0330003
10. E. R. Wainwright, F. De Lucia, T. P. Weihs, and J. L. Gottfried, *Spectrochim. Acta B*, 2021, **183,** 106270. https://doi.org/10.1016/j.sab.2021.106270
11. Z. Wang, Y. Li, Y. Chen, and R. Li, *Spectrochim. Acta, Part B*, 2025, **226,** 107139. https://doi.org/10.1016/j.sab.2025.107139
12. Z. Li, Q. Zhang, L. Kong, G. Lian, and J. Yang, *Heat Treat. Met*., 2022, **47,** 284-290. https://doi.org/10.13251/j.issn.0254-6051.2022.01.048
13. B. W. Xue, M. C. Cui, C. X. Wang, Z. F. Miao, P. Liao, and S. D. Zhao, *Laser Technol*., 2018, **42,** 806-810. https://doi.org/10.7510/jgjs.issn.1001-3806.2018.06.015
14. S. Smetaczek, A. Limbeck, V. Zeller, J. Ring, S. Ganschow, D. Rettenwander, and J. Fleig, *Mater. Adv*., 2022, **3,** 8760-8770. https://doi.org/10.1039/d2ma00845a
15. C. Burgos-Palop, P. Purohit, F. J. Fortes, and J. Laserna, *Anal. Chem*., 2023, **95,** 14541-14550. https://doi.org/10.1021/acs.analchem.3c01376
16. P. D. Lei, H. B. Fu, D. R. Yi, J. W. Yang, and L. H. Kong, *Chin. J. Lasers*, 2020, **47**, 293-301. https://doi.org/10.3788/CJL202047.0411001
17. L. X. Sun, W. Wang, X. Y. Tian, P. Zhang, L. F. Qi, and L. M. Zheng, *Chin. J. Anal. Chem*., 2018, **46**, 1518-1527. https://doi.org/10.11895/j.issn.0253-3820.181150
18. S. Wold, M. Sjöström, and L. Eriksson, *Chemometr. Intell. Lab. Syst*., 2001, **58,** 109-130. https://doi.org/10.1016/S0169-7439(01)00155-1
19. K. Fatima, N. Ahmed, R. Khan, Z. A. Umar, M. A. Baig, K. Althubeiti, S. A. Otaibi, S. Abdullaev, and N. Elboughdiri, *Chem. Phys. Impact*, 2025, **10,** 100884. https://doi.org/10.1016/j.chphi.2025.100884
20. F. W. Khan, R. Ahmed, M. Rafique, J. Iqbal, M. A. Baig, and N. *Ahmed, Laser Phys*., 2025, **35,** 075701. https://doi.org/10.1088/1555-6611/adebec
21. G. De Temmerman, T. W. Morgan, G. G. Van Eden, T. De Kruif, M. Wirtz, J. Matejicek, T. Chraska, R. A. Pitts, and G. M. Wright, *J. Nucl. Mater*., 2015, **463**, 198-201. https://doi.org/10.1016/j.jnucmat.2014.09.075
22. A. Ghazari, C. McElfresh, D. Dickstein, W. Nadvornick, G. Pintsuk, E. Wessel, M. Wirtz, D. Hughes, B. Williams, J. Marian, and N. Ghoniem, *J. Nucl. Mater*., 2022, **565,** 153730. https://doi.org/10.1016/j.jnucmat.2022.153730
23. Z. Gong, L. Yang, Y. Cao, J. Liu, and S. Zhou, *Mater. Today Commun*., 2025, **46,** 112532. https://doi.org/10.1016/j.mtcomm.2025.112532
24. H. Ni, *Explosion Shock Waves*, 2024, **44,** 118-126. https://doi.org/10.11883/bzycj-2023-0262
25. S. Zhang, C. Shi, B. Wang, S. Ding, L. Wang, P. Gu, Z. Zhang, and H. Zhang, *Jpn. J. Appl. Phys*., 2025, **64,** 081003. https://doi.org/10.35848/1347-4065/adf7f4
26. F. H. Stillinger, *Phys. Rev. B*, 2005, **71,** 024301. https://doi.org/10.1103/PhysRevB.71.024301
27. T. Krauskopf, S. Muy, S. P. Culver, S. Ohno, O. Delaire, Y. Shao-Horn, and W. G. Zeier, *J. Am. Chem. Soc*., 2018, **140,** 14464-14473. https://doi.org/10.1021/jacs.8b09340
28. J. -M. Albina, C. Elsässer, J. Weissmüller, P. Gumbsch, and Y. Umeno, *Phys. Rev. B*, 2012, **85,** 125118. https://doi.org/10.1103/PhysRevB.85.125118
29. P. Rez, T. Boland, C. Elsässer, and A. Singh, *Microsc. Microanal*., 2022, **28**, 672-679. https://doi.org/10.1017/S143192762200040X
30. K. Li, Z. Zhang, Z. Lin, Y. Zhang, C. Liu, H. Wu, Y. Zhu, and H. Ma, *ACS Nano*, 2026, **20**, 11284-11293. https://doi.org/10.1021/acsnano.6c00656